

# Ion and Solvent Dynamics in Charged 2D Clay Nanoslits with Unprecedented Ångström-Precise Slit Height Control

Max Stevenson, Sandra Pappler, Leonie Kanzler, Aqsa Nisar, Jepsinraj Kakkuzhiyulla Parambath, Markus Rosenstihl, Flora Lebeda, Sebastian Weiß, Georg Papastavrou,\* Michael Vogel,\* Jürgen Senker,\* and Josef Breu\*

\_Nanofinement by layered silicates has been claimed to deliver superionic conductivity as needed for many electrochemical applications. Unraveling governing principles of solvent and ion dynamics within charged 2D nanochannels requires Å-precise slit height control. This work addresses existing experimental limitations utilizing synthetic fluorohectorite, known for its superb homogeneous charge distribution, high aspect ratio (> 20,000), and spontaneous delamination by 1D-dissolution. This triad of properties enables an Å-precise slit height control of monodomain Bragg stack membranes over a wide slit height range (5–100 Å) while offering a variable and high surface charge (0.17–0.24 C m<sup>-2</sup>). A concerted characterization applying electrochemical impedance spectroscopy (EIS), colloidal-probe atomic force microscopy (CP-AFM), pulsed- and static-field gradient nuclear magnetic resonance (PFG- and SFG-NMR), assisted by molecular dynamics (MD) simulations, revealed in-depth insights: The maximum conductivity (0.2 S m<sup>-1</sup>) is observed at a confinement of 15.1 Å, where aside of the two Helmholtz planes (HP) attached to the confinement walls a diffuse layer (DL) exists. Independent of the surface charge, the vast majority of Li<sup>+</sup> is strongly bound by electrostatics and hydrogen bonding of the first hydration shell to the anionic walls. Regardless of the slit height and electrolyte concentration, conductivity is governed by the Li<sup>+</sup> balancing the surface charge.

processes.<sup>[1–9]</sup> Understanding, controlling, and optimizing individual selective ionic and molecular transport mechanisms enabled rapid advancements in various technological sectors such as electrochemical energy storage,<sup>[10]</sup> energy conversion,<sup>[11]</sup> energy harvesting,<sup>[12]</sup> bio-sensing,<sup>[13,14]</sup> water purification,<sup>[15]</sup> and molecular/ion sieving.<sup>[16]</sup> Particular research interest has been dedicated to the governing principles of superionic conductivities within nanochannels of 2D materials.<sup>[17,18]</sup>

A plethora of synthesis and preparation routes for nanostructured 2D materials have been explored over the years.<sup>[19,20]</sup> However, they typically lack either 1) variability and tunability or 2) scalability. The approaches limit systematic variations of governing parameters that are key to a deeper understanding. The crucial parameters governing the angstrom and nanoscale transport of ions and molecules within these nanochannels<sup>[21–23]</sup> are 1) the slit height, 2) the charge density of the confining surfaces, 3) the ion type and valency, 4) the solvent, and lastly 5) the ionic strength of confined electrolytes.

The principles of ion and solvent mobility in confinement are well-founded in their theoretical concepts.<sup>[24,25]</sup> However, experimental confirmation is still incomplete. The most precise control for experimental confinement parameters is achieved with a

## 1. Introduction

Nanopores and nanochannels of different dimensionalities (0D, 1D, 2D, and 3D) are vital in various biological and technological

M. Stevenson, S. Pappler, L. Kanzler, F. Lebeda, S. Weiß, G. Papastavrou, J. Senker, J. Breu  
Department of Chemistry  
University of Bayreuth  
Universitätsstraße 30, 95447 Bayreuth, Germany  
E-mail: Georg.Papastavrou@uni-bayreuth.de;  
Juergen.Senker@uni-bayreuth.de; Josef.Breu@uni-bayreuth.de

M. Stevenson, S. Pappler, L. Kanzler, F. Lebeda, S. Weiß, G. Papastavrou, J. Senker, J. Breu  
Bavarian Center for Battery Technology (BayBatt)  
University of Bayreuth  
Universitätsstraße 30, 95447 Bayreuth, Germany  
A. Nisar, J. K. Parambath, M. Rosenstihl, M. Vogel  
Institute for Condensed Matter Physics  
Technical University Darmstadt  
Hochschulstraße 6, 64289 Darmstadt, Germany  
E-mail: michael.vogel@pkm.tu-darmstadt.de

The ORCID identification number(s) for the author(s) of this article can be found under <https://doi.org/10.1002/adfm.202515706>

© 2025 The Author(s). Advanced Functional Materials published by Wiley-VCH GmbH. This is an open access article under the terms of the [Creative Commons Attribution](#) License, which permits use, distribution and reproduction in any medium, provided the original work is properly cited.

DOI: 10.1002/adfm.202515706

Top-Down fabrication of individual nanochannels by assembling two coplanar surfaces pillared to desired distances.<sup>[26]</sup> This approach was optimized over the years to Å-precision<sup>[27]</sup> but is restricted to uncharged or low-charged 2D materials (Graphene, hBN, MoS<sub>2</sub>). Moreover, as only individual channels are measured, the signal-to-noise ratio of conventional characterization techniques represents a severe challenge.

Bottom-up formation of nanochannels is a less sophisticated and more common experimental approach, where dispersed mono- and multilayer nanosheets are self-assembled into membranes with approximately coplanar arrangement.<sup>[28]</sup> This approach offers the advantage of simultaneously generating a large number of channels, albeit less ordered. A variety of 2D materials (vermiculites, GO, MoS<sub>2</sub>, MXene, LDHs)<sup>[29–33]</sup> have been utilized with applications like water purification,<sup>[16]</sup> osmotic power generation,<sup>[34]</sup> or battery separators<sup>[35,36]</sup> in mind. The downside of this approach lies in the lack of control over the height of the 2D building blocks. With multilayer nanosheets of different thicknesses, the height of the self-assembled slits will vary. Uniform slit heights require suspensions of mutually repelling monolayers with subsequent membrane self-assembly. Once these are assembled, the slit height must be controlled by incorporation of pillars or by solvation (swelling).<sup>[37,38]</sup>

Strictly monolayers are only obtained by thermodynamically driven, spontaneous delamination of ionic 2D materials. This process is referred to as 1D dissolution.<sup>[39]</sup> As the number of layered materials that can be delaminated by 1D dissolution steadily increases, a modular toolbox has become available to fabricate membranes with utter confinement control. For these materials, delamination is driven by the electrostatic repulsion of adjacent layers, and nematic liquid crystalline suspensions are obtained. The separation of the coplanar nanosheets is controlled by the volume ratio of nanosheets and the dispersant, and the ionic strength. Separations up to the Debye length represent Wigner crystals, where repelling individual nanosheets are kept in a 1D crystalline arrangement of coplanar nanosheets. When fabricating membranes from these nematic suspensions, monodomain Bragg stacks are obtained. The separation of the nanosheets in these monodomains may easily be tuned over a substantial range by adding various amounts of swelling solvents/electrolytes to the Wigner-type monodomain.

Here, we fabricate such Wigner-type, monodomain Bragg stack membranes with nematic suspensions of lithium fluorohectorite [Li<sub>x</sub>]<sup>inter</sup>[Mg<sub>3-x</sub>Li<sub>x</sub>]<sup>oct</sup>[Si<sub>4</sub>]<sup>tet</sup>O<sub>10</sub>F<sub>2</sub> (Li<sub>x</sub>Hec, x = 0.5 or 0.7), which were obtained by ion exchange from the Na<sub>x</sub>Hec (Figures S1–S4, Supporting Information).

Swelling the membranes with different aliquots of aqueous dispersant produces nanoconfinements ranging from 2 to 250 Å. Moreover, the number of slits of a dried membrane of 50 μm thickness is 50000. Slit heights within the membrane are uniform and can be controlled with Å-precision, easing the problem of signal-to-noise ratio. Mobility in confinement may thus be measured for bulk samples instead of individual channels. The ionic conductivity across varying confinements was measured by electrochemical impedance spectroscopy (EIS) and compared to pulsed- and static-field gradient nuclear magnetic resonance spectroscopy (PFG-/SFG-NMR). The latter, moreover, allows studying the degree of displacements for Li<sup>+</sup> and water molecules and their correlated transport. Additional insights into

local dynamics were obtained through NMR lineshape analysis and longitudinal relaxation time measurements. Molecular dynamics (MD) simulations further modeled ion and solvent behavior, while colloidal probe atomic force microscopy (CP-AFM) characterized the diffuse properties of the nanosheet surfaces.

## 2. Results and Discussion

### 2.1. Fabrication of Membranes and EIS Characterization

Fluorohectorite, a 2:1 layered silicate, was obtained through melt synthesis and subsequent long-term annealing, which ensures a uniform charge density.<sup>[40,41]</sup> The very large platelet diameter of the pristine crystals (Figure 1a) transforms into huge aspect ratios upon delamination into monolayer nanosheets (1 nm thin).

Upon casting the randomly oriented nematic liquid crystal domains (Figure 1b) on a planar substrate, membranes of overlapping perfectly parallel aligned nanosheets are produced (Figure 1c). The excellent 1D crystallinity is reflected in an X-ray diffractogram (Figure 1e) that resembles a single-domain diffraction pattern. As swollen Wigner-type Bragg stack membranes slowly evaporate water at the surface, gradient materials will be obtained if measured without a gas-tight container. The container must allow for small-angle X-ray diffraction (XRD) in Bragg-Brentano geometry to determine the exact slit height, confocal laser-scanning microscopy (CLSM) to determine the membrane thickness, and EIS to measure the ionic conductivity. To meet these requirements, a purposely constructed in situ cell was used (Figure 1d). The cell was carefully and tightly sealed with high vacuum grease to prevent water evaporation, and the slit height was cross-checked with XRD before and after all measurements, to assure a stable and reproducible slit height during measurements (< 8 h).

The slit height (Figure 1e) is determined from the 00*l*-series observed for the Bragg stack membrane. The periodicity in the stacking direction comprises the thickness of the 2:1 silicate monolayer (≈10 Å) and the slit containing solvated cations and water molecules. Narrow slits with a slit height of 2.4 and 5.6 Å are produced by equilibrating the membranes at relative humidities of 43% and 95%, respectively. The slit dimensions correlate to the kinetic diameter of a water molecule (2.68 Å<sup>[42,43]</sup>) and can only be varied in steps of integral numbers of “water layers” (WL). Homogeneity of the charge density is a prerequisite for uniform swelling with water. Melt-synthesized Li<sub>x</sub>Hec allows for achieving slit heights corresponding with up to 6 WL (2.4, 5.6, 8.5, 11.8, 15.1, 18.2 Å) (Figures S5–S7, Supporting Information). In this range, distinct steps of slit confinement are observed. The 00*l*-series is highly rational, indicating that each slit has the same height with perfect translational periodicity across the domain. As already reported by Israelachvili and Pashley,<sup>[43]</sup> at higher swelling commencing at 7 WL (> 21.4 Å), the repulsion of adjacent nanosheets apparently is no longer strong enough to strictly determine the number of water layers in individual confinements. Some slit heights then randomly vary by one water layer; consequently, the X-ray beam averages over the varying periodicities in a number-weighted fashion. As a result, the apparent slit height appears to shift in a quasi-continuous manner rather than in discrete, stepwise increments (Figure S7c, Supporting Information). Moreover, these randomly interstratified

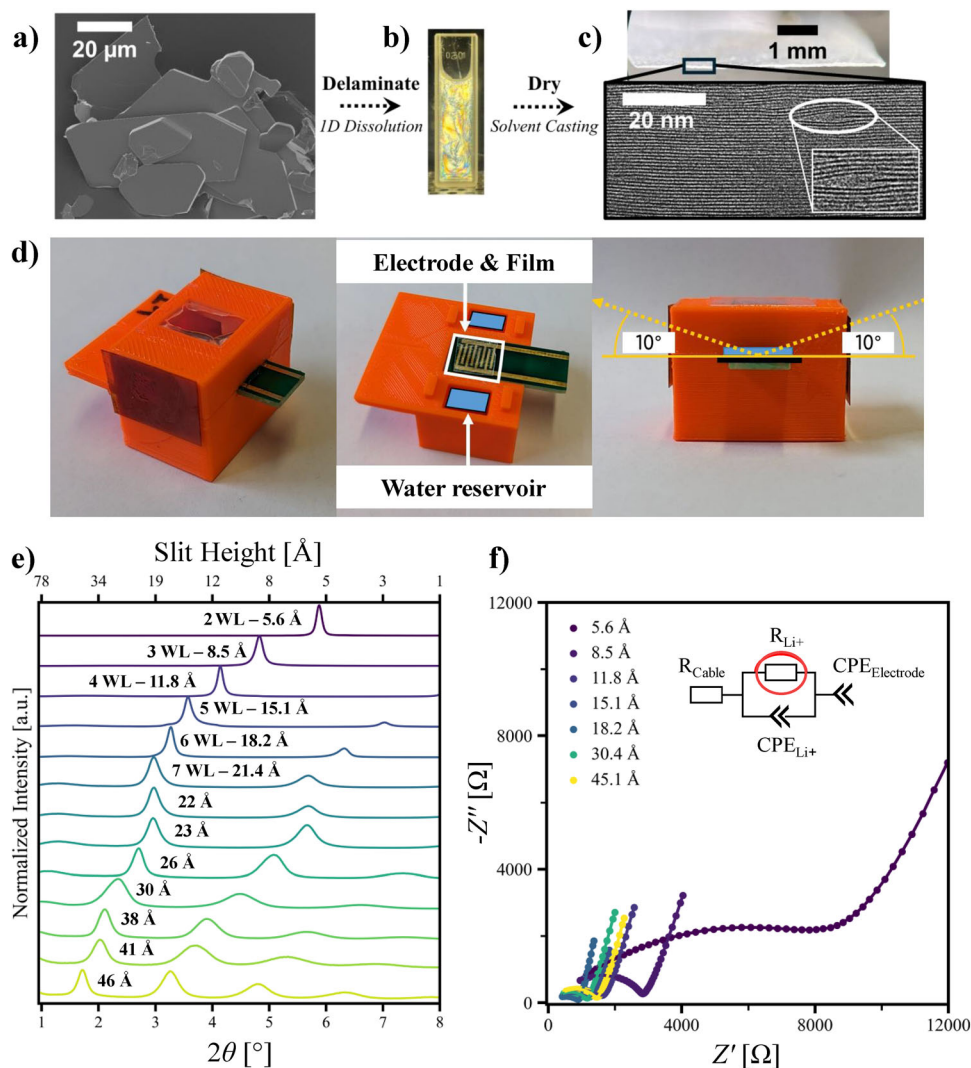


**Figure 1.** Schematic representation of material processing. Membranes with coplanar aligned nanosheets of fluorohectorite were prepared by spontaneously delaminating a) micron-sized platy crystals into a b) birefringent nematic suspension of coplanar 1 nm thick nanosheets. The nematic suspension is degassed, solvent cast, and dried to obtain c) textured monodomain Bragg stack membranes of 50  $\mu\text{m}$  thickness, typically comprising 50000 nanosheets/slits. Picture of the macroscopic membrane (top) and transmission electron micrograph (TEM, bottom) of the cross-section of such a membrane. Individual nanosheets are highly flexible and close the gap caused by an ending nanosheet within a few nanometers. Due to the large aspect ratio of overlapping nanosheets, these local defects are scarce and may be neglected for the bulk properties of the membrane. d) Homemade in situ cell setup consisting of a bottom compartment with water reservoirs to maintain 100% r.h., an interdigitated electrode (IDE) with a finger width and distance of 500  $\mu\text{m}$  for EIS measurements, a 50  $\mu\text{m}$  thick  $\text{Li}_{0.5/0.7}\text{Hec}$  membrane, Kapton foil closed side windows for small-angle Bragg-Brentano geometry XRD measurements of up to  $10^\circ$   $2\theta$ , and a top component with a transparent glass slide for CLSM membrane thickness measurements. e) XRD patterns of different degrees of  $\text{Li}_{0.5}\text{Hec}$  hydration and the respective slit heights. f) Exemplary EIS measurements of the hydrated  $\text{Li}_{0.5}\text{Hec}$  samples. Refinement was performed with the depicted circuit diagram. The refined diameter of the semicircle was the ionic resistance.

defects in the periodicity cause a substantial reduction of peak intensities and a peak broadening. The membrane thickness obtained after swelling was measured as the height difference of the electrode substrate with the membrane surface via CLSM (Figure S8, Supporting Information). EIS (Figure 1f; Figure S9, Supporting Information) was applied for monodomain Bragg stack membranes on an interdigitated electrode (IDE, Figures S10–S13, Supporting Information) in the frequency range of  $10^2$ – $10^6$  Hz with an excitation voltage of 10 mV to determine ion conductivity. The data was refined with a simple electrical circuit

using “RelaxIS”. The circuit is a variation of a Randles circuit. It consists of a resistor ( $R_{\text{Cable}}$ ), in series with a parallel resistor ( $R_{\text{Li}^+}$ ) and a constant phase element ( $\text{CPE}_{\text{Li}^+}$ ), and in series with one last constant phase element ( $\text{CPE}_{\text{Electrode}}$ ).  $R_{\text{Cable}}$  is not the solution resistance, but the cable connection, which ranges from 0 to 200  $\Omega$  depending on the crocodile clamp positioning. The parallel  $R_{\text{Li}^+}$  and  $\text{CPE}_{\text{Li}^+}$  refer to the ionic process, with the fitted diameter of the semicircle  $R_{\text{Li}^+}$  as the  $\text{Li}^+$  conductance (S) of the membrane. Lastly,  $\text{CPE}_{\text{Electrode}}$  is the capacitive blocking electrode interface.

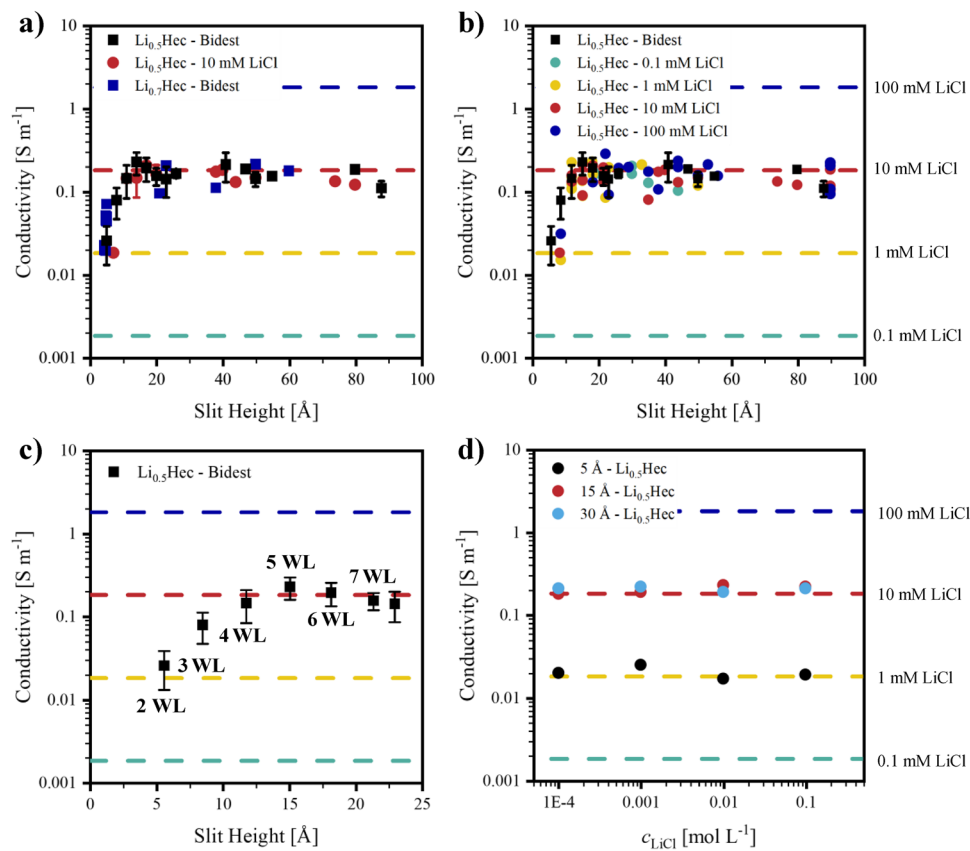


**Figure 2.** Conductivity as a function of slit height for a) two different layer charges  $\text{Li}_x\text{Hec}$  ( $x = 0.5/0.7$ ) swollen with bidistilled (bidest.) water, as well as  $\text{Li}_{0.5}\text{Hec}$  swollen with an aq. 10 mM LiCl electrolyte. b)  $\text{Li}_{0.5}\text{Hec}$  swollen with aqueous electrolytes of varying LiCl concentration (0.1–100 mM). c) Close-up of the initial hydration steps of  $\text{Li}_{0.5}\text{Hec}$  swollen with bidest. water. d) Conductivity of electrolytes as a function of varying LiCl concentration (0.1–100 mM). Markers with error bars indicate averaged values and the respective standard deviation of at least five values of the same slit height. Dashed horizontal lines indicate the conductivity of aqueous electrolytes with the respective LiCl concentration.

## 2.2. Conductivity as a Function of Slit Height

Combining the results of the three techniques (XRD, EIS, and CLSM) allows the determination of the conductivity ( $\text{S m}^{-1}$ ) as a function of variable slit height. The experimental section and the Supporting Information discuss the analysis of EIS data, CLSM measurements, and the resulting conductivity calculation in more detail.

The slit-height-dependent conductivity (Figure 2a) while swelling with bidistilled (bidest.) water was determined for two different layer charges ( $\text{Li}_{0.5}\text{Hec}$ ,  $0.17 \text{ C m}^{-2}$ ,  $2.2 \text{ Li}^+ \text{ nm}^{-2}$ ; and  $\text{Li}_{0.7}\text{Hec}$ ,  $0.24 \text{ C m}^{-2}$ ,  $3.0 \text{ Li}^+ \text{ nm}^{-2}$ ). The layer charges were derived from unit cell parameters and composition (Section S2.4.2, Supporting Information). Control of the slit height relies on the Wigner crystal nature of the membrane. When the charge density is increased above  $0.24 \text{ C m}^{-2}$ , the Coulomb attraction leads to a collapse of the slits, as the repulsive interaction at the base of the Wigner crystal is turned attractive. Thus,  $0.24 \text{ C m}^{-2}$  is the upper surface charge density limit for slit height control of the fluorohectorite. Literature reported increased conductivity with increasing surface charge density.<sup>[26,44]</sup> In the same line, theoretical modeling<sup>[24]</sup> predicted a 40% increase in conductivity with increased charge density. Contrary to these reports, we found the absolute conductivity and its trend to be identical within experi-

mental error for the two different layer charge densities. As the slit height increases, the conductivity rises from  $0.02 \text{ S m}^{-1}$  at a slit height of  $5.6 \text{ \AA}$  to a maximum of  $0.2 \text{ S m}^{-1}$  at  $15.1 \text{ \AA}$  (5 WL) (Figure 2c). This maximum is followed by a plateau of slightly but insignificantly lower conductivity as the slit height is further increased up to  $90 \text{ \AA}$ , where the conductivity was found to be  $0.15 \text{ S m}^{-1}$ . Only for very dilute suspensions of randomly oriented nematic domains with 1 wt.% (180 nm slit height) and 0.1 wt.% (1800 nm slit height), much-reduced conductivities of  $0.025 \text{ S m}^{-1}$  and  $0.003 \text{ S m}^{-1}$  were found, respectively. Both these dilute suspensions are way out of the Wigner crystal regime.<sup>[45]</sup>

The initial steep increase in conductivity is in accordance with observations reported for other swelling 2D materials, such as clays<sup>[46]</sup> and  $\text{Li}_{0.8}\text{Sn}_{0.8}\text{S}_2$ .<sup>[37]</sup> The high conductivity of  $0.2 \text{ S m}^{-1}$  within the slits, which is substantially higher than the measured conductivity of bidest. water ( $20 \mu\text{S m}^{-1}$ ), is also in accordance with theoretical models and experimental observations for ion transport in charged nanochannels.<sup>[24,26]</sup>

Swelling the membranes with aqueous electrolytes of varying LiCl concentration (0.1–100 mM) (Figure 2b,d) gave the same dependency on slit height and the same conductivity at a given slit height regardless of the electrolyte concentration. This independence of concentration was surprising, as previous reports suggested a linear increase of conductivity

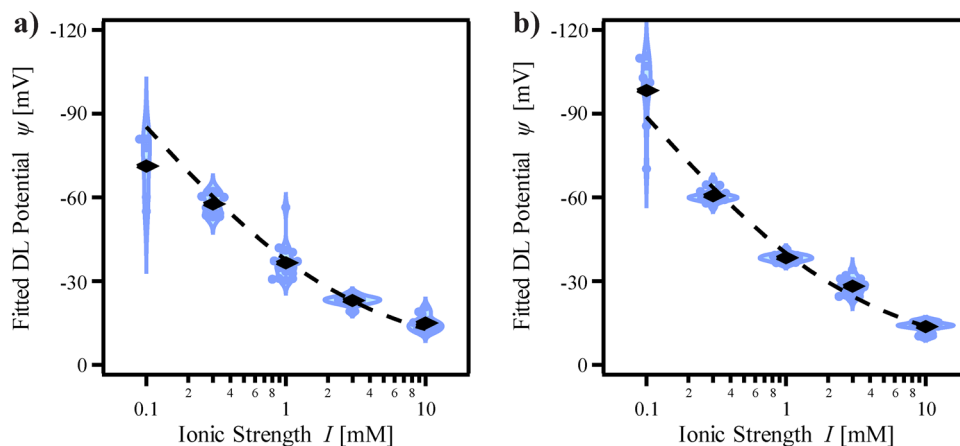


**Figure 3.** Fitted DL potentials as a function of electrolyte ionic strength for two different layer charges of a)  $\text{Li}_{0.5}\text{Hec}$  and b)  $\text{Li}_{0.7}\text{Hec}$ . Blue dots correspond to the averaged measurements at a single spot. Black diamonds indicate the mean DL potential for each ionic strength. The dashed line represents a fit to the Grahame equation, relating the DL potential to ionic strength.

resembling bulk electrolyte behavior at electrolyte concentrations ( $> 10 \text{ mM}$ ).<sup>[26,29,30,32,44]</sup> For both charge densities, the externally added  $\text{Li}^+$  from the electrolyte is orders of magnitude lower than the slits intrinsic concentration of  $\text{Li}^+$  required to balance the surface charge of the anionic hectorite nanosheets. A more detailed discussion will be provided in Sections 2.6 and 2.7.

### 2.3. Diffuse Layer Properties by Direct Force Measurements

The charge density of the nanosheets and, hence, the number of  $\text{Li}^+$  interlayer cations balancing this charge can easily be varied by increasing the degree of isomorphic substitution of octahedral cations. Going from  $\text{Li}_{0.5}\text{Hec}$  to  $\text{Li}_{0.7}\text{Hec}$  increases the total number of interlayer  $\text{Li}^+$  by 40%. At the same time, this increase in charge density of the confining silicate walls will severely influence both the distribution of  $\text{Li}^+$  across the slit and their mobility.

The diffuse layer (DL) properties, and thus the ion distribution in  $\text{Li}_{0.5}\text{Hec}$  and  $\text{Li}_{0.7}\text{Hec}$  in  $\text{Li}^+$ -containing electrolytes, can be probed by direct force measurements (Figures S14 and S15, Supporting Information) using the colloidal probe technique based on atomic force microscopy.<sup>[47–49]</sup> The corresponding measurements were performed in aqueous  $\text{LiCl}$  solutions of varying ionic strengths. The experimental force-distance data were evaluated by fitting the full solutions of the Poisson–Boltzmann equation using the constant regulation approximation, allowing extraction of the diffuse layer potential ( $\psi$ ), the regulation parameter ( $p$ ) (Figure S16, Supporting Information), and the Debye length ( $\kappa^{-1}$ ).<sup>[50–52]</sup> These values were then used to calculate the diffuse layer charge density ( $\sigma_{\text{DL}}$ ) via the Grahame equation, which relates the DL potential to the ionic strength.

Figure 3a,b shows the fitted DL potentials as a function of ionic strength for two different layer charges of  $\text{Li}_{0.5}\text{Hec}$  ( $0.17 \text{ C m}^{-2}$ ) and  $\text{Li}_{0.7}\text{Hec}$  ( $0.24 \text{ C m}^{-2}$ ). Further details on the interpretation of force-distance data, the Poisson–Boltzmann analysis, and the application of the Grahame equation are provided in the Supporting Information. By fitting the Grahame equation over the full range of ionic strengths,<sup>[51,52]</sup> DL charge densities of

$\sigma_{\text{DL}} = (2.96 \pm 0.16) \times 10^{-3} \text{ C m}^{-2}$  for  $\text{Li}_{0.5}\text{Hec}$  and  $\sigma_{\text{DL}} = (3.12 \pm 0.11) \times 10^{-3} \text{ C m}^{-2}$  for  $\text{Li}_{0.7}\text{Hec}$  were obtained.

The direct force measurements by AFM indicate that  $\text{Li}_{0.5}\text{Hec}$  and  $\text{Li}_{0.7}\text{Hec}$  have a comparable diffuse layer potential. This observation can be attributed to differences in specific ion adsorption within the inner and outer Helmholtz planes (IHP and OHP), which contribute to the overall DL charge density and may vary with surface charge. In the context of the  $\text{Li}^+$  distribution within hectorite slits at slit heights  $> 2$  OHP, one may conclude that although  $\text{Li}_{0.7}\text{Hec}$  hosts a higher total ion concentration, a larger fraction of these ions is less mobile within the IHP and OHP than in the diffuse layer. The ratio of diffuse layer charge density to nominal surface charge density is  $\approx 1.74 \times 10^{-2}$  ( $0.17 \text{ C m}^{-2}$  vs  $2.96 \times 10^{-3} \text{ C m}^{-2}$ ) for  $\text{Li}_{0.5}\text{Hec}$  and  $1.30 \times 10^{-2}$  ( $0.24 \text{ C m}^{-2}$  vs  $3.12 \times 10^{-3} \text{ C m}^{-2}$ ) for  $\text{Li}_{0.7}\text{Hec}$ . Thus, only a minority of  $\text{Li}^+$  in the slit resides in the DL.

### 2.4. Distribution of $\text{Li}^+$ Across the Slit as Probed by Poisson–Boltzmann and Molecular Dynamics Simulations

As the colloidal probe technique focuses on a single nanosheet surface rather than a slit confined between two coplanar nanosheets, Poisson–Boltzmann<sup>[53]</sup> (PB, Figure S17, Supporting Information) and MD simulations<sup>[54,55]</sup> were applied to cross-check this distribution. Both approaches confirm that the vast majority of cations in the slit reside in the OHP. Only a small fraction of cations is located within the DL, remote from the confining surfaces, where they are expected to be more mobile due to reduced surface interactions. As has been shown by Rotenberg et al.,<sup>[54]</sup> the simplistic PB model gave accuracies comparable to more sophisticated MD simulations. By setting the cutoff between Helmholtz planes (HP) and DL compartments at  $4 \text{ \AA}$  from the surface ( $1.5 \text{ WL}$ ) and calculating the cation distribution for  $\text{Li}_{0.5}\text{Hec}$  at a slit height of  $25 \text{ \AA}$  using PB theory, it was found that 31 % of  $\text{Li}^+$  cations reside in the DL. As the slit height increases, this fraction of  $\text{Li}^+$  within the DL increases to 35 % at a slit height of  $69 \text{ \AA}$ , where it levels off. Although all  $\text{Li}^+$  within the slit are mobile, as will be shown by MD simulations,  $\text{Li}^+$  residing

within the DL are considered somewhat faster. For  $\text{Li}_{0.7}\text{Hec}$ , the ratio of  $\text{Li}^+$  residing in the DL decreases to 25 % and 28 %, respectively. This implies that with increased surface charge, despite the 40 % increase in total interlayer  $\text{Li}^+$ , the number of cations in the DL increases as little as 12 % ( $28 \% \times 0.24 \text{ C m}^{-2}$  vs  $35 \% \times 0.17 \text{ C m}^{-2}$ ). This implication aligns with the CP-AFM observations of a  $\approx 5\%$  increase in DL charge density. As a result, the conductivities of  $\text{Li}_{0.5}\text{Hec}$  and  $\text{Li}_{0.7}\text{Hec}$  do not differ within experimental error.

Spatially resolved insights into the structure and dynamics of slit constituents were obtained by MD simulations (Figure S18, Supporting Information). These were carried out for  $\text{Li}_{0.5}\text{Hec}$  and slit heights of 7.2 and 69 Å (Figure 4). While the first simulation falls in the regime where the ionic conductivity increases steeply, the second falls in the regime of the conductivity plateau (Figure 2a). The number density profiles  $n_{\text{perp}}(z)$  of  $\text{Li}^+$  and water oxygen atoms ( $\text{O}_{\text{W}}$ ), resolved along the  $z$ -direction perpendicular to the hectorite surfaces, are shown in Figure 4a,b. For the small slit height of 7.2 Å, two distinct  $\text{Li}^+$  layers are observed, each separated from the respective hectorite surface by a well-defined water layer, as expected for OHP formation. Moreover, there is a third water layer in the center of the slit. These findings are similar to prior MD simulations of 3 WL of the sodium fluorohectorite.<sup>[45]</sup>

For the large slit height of 69 Å (Figure 4b), we focus on just one of the two confining interfaces as the structure is symmetrical. The majority of  $\text{Li}^+$  is located in a layer adjacent to the hectorite surface, corresponding to the OHP ( $< 4$  Å, 65%). Additionally, a second smaller maximum is observed and attributed to the DL ( $4 \text{ Å} < z < 7 \text{ Å}$ ). While PB assumes a continuous decrease in the  $\text{Li}^+$  concentration profile, an atomistic model such as MD instead locates the cations between discrete layers of water, resulting in a non-monotonous decrease of the  $\text{Li}^+$  concentration across the slit. The first  $\text{O}_{\text{W}}$  (Figure 4b,e) coordinating to  $\text{Li}^+$  and the first  $\text{Li}^+$  maximum (Figure 4b,f) are found at  $\approx 1.3$  and  $2.4$  Å from the hectorite surface, respectively. As indicated by the presence of a shoulder, this  $\text{O}_{\text{W}}$  layer is somewhat corrugated, reflecting that the underlying plane of basal oxygens is not densely packed but instead forms a Kagome net structure (Figure 4c). Moreover, the Coulomb interaction is different for monovalent  $\text{Li}^{\text{oct}}$  and divalent  $\text{Mg}^{\text{oct}}$ , which also leads to some corrugation. Further away from the confinement wall is a transition zone with less pronounced maxima before the number density becomes independent of the  $z$  position at  $z \approx 9$  Å, corresponding to 3 WL. When 3 WL at each surface are considered, the positions of the  $\text{O}_{\text{W}}$  maxima in Figure 4b align with the expected midpoints of the water layers, as observed by XRD and shown in Figure 1e.

In the  $(x,y)$  plane, water molecules of the first  $z$  layer reside at two different positions. A fraction ( $0.2 \text{ Å} \leq z < 0.6 \text{ Å}$ ) occupies the hexagonal cavities on the hectorite surface (Figure 4d). Another fraction ( $1.2 \text{ Å} \leq z < 1.6 \text{ Å}$ ) interacts with the basal oxygens of the tetrahedral layer ( $\text{O}_{\text{S}}$ ), leading to a hexagonal symmetry (Figure 4e). At any given instant, typically only three of the six equivalent positions occupied by water molecules coordinate to the partially filled  $\text{Li}^+$  position at  $1.8 \text{ Å} \leq z < 2.2 \text{ Å}$  residing above the hexagonal cavities, in line with published single crystal data (Figure 4f; Figure S5, Supporting Information). When increasing the distance from the confinement wall, the structuring becomes less prominent, but the epitaxial effects of the confinement structure extend well into the slit. In particular, the  $(x,y)$  positions of

the  $\text{O}_{\text{W}}$  (Figure 4g) and  $\text{Li}^+$  (Figure 4h) at  $3 \text{ Å} < z < 4 \text{ Å}$  still reflect the arrangement of the basal oxygens. Hence, the water molecules do not adopt the tetrahedrally coordinated structures typical of bulk water.

Next, the  $\text{Li}^+$  and water diffusion along the interlayer was studied based on 2D mean squared displacements (Equation S18, Supporting Information) for a slit height of 69 Å. In these simulations, we distinguish between  $\text{Li}^+$  and  $\text{O}_{\text{W}}$ , as well as between different  $z$ -starting positions of the diffusion process relative to the hectorite surface. In Figure 4i, we see that for  $t \leq 10^4$  ps,  $\text{Li}^+$  initially located at  $0 \text{ Å} < z < 4 \text{ Å}$  exhibit smaller displacements than those starting further away from the hectorite surface. However, the 2D mean squared displacements of  $\text{Li}^+$  with different  $z$ -starting intervals differ at most by a factor of  $\approx 2$ . Hence, differences in  $\text{Li}^+$  mobilities are small. At times  $t > 10^4$  ps, all fractions show identical displacement values, indicating an exchange of  $\text{Li}^+$  between the OHP and the DL volume.  $\text{O}_{\text{W}}$  displays similar behavior, as shown in Figure 4j. While the  $\text{O}_{\text{W}}$  displacements depend on the initial position at sufficiently short time and length scales, quantitative differences in their mobility are smaller than for  $\text{Li}^+$ . Furthermore, different merging points of the curves indicate that the exchange between different spatial regions is faster for  $\text{O}_{\text{W}}$  than for  $\text{Li}^+$ . Self-diffusion coefficients of  $\text{Li}^+$  ( $D_{\text{Li}}$ ) and  $\text{O}_{\text{W}}$  ( $D_{\text{Ow}}$ ) can be obtained by fitting the common long-time behavior. For the slit height of 69 Å, diffusivities of  $D_{\text{Li}} = 8.1 \times 10^{-10} \text{ m}^2 \text{ s}^{-1}$  and  $D_{\text{Ow}} = 2.5 \times 10^{-9} \text{ m}^2 \text{ s}^{-1}$  are obtained. In line with the observed steep increase of ion conductivity, the respective self-diffusion coefficients are substantially smaller for a slit height of 7.2 Å and amount to  $D_{\text{Li}} = 4.0 \times 10^{10} \text{ m}^2 \text{ s}^{-1}$  and  $D_{\text{Ow}} = 1.0 \times 10^{-9} \text{ m}^2 \text{ s}^{-1}$ . Thus, for both slit heights, the water molecules diffuse faster than the  $\text{Li}^+$ .

MD simulations support colloidal probe measurements and PB simulations by demonstrating that most  $\text{Li}^+$  ( $\approx 65\%$ ; both derived by MD and PB) reside close to the hectorite surface. Only  $\approx 35\%$  of  $\text{Li}^+$  may be attributed to the DL. While  $\text{Li}^+$  in the OHP are more strongly confined by hydrogen bonding of the first coordination shell to the basal oxygens of hectorite, all  $\text{Li}^+$  are mobile. Fast exchange between the different sites ensures that all  $\text{Li}^+$  contribute to the ionic conductivity. The  $\text{Li}^+$  cations for both MD models (7.2 and 69 Å) are octahedrally coordinated by water molecules. As HPs exist on both sides of the slit confinement, amounting to a thickness of  $\approx 11.2$  Å, the 4 WL slit represents the minimum slit separation where the first coordination shell of  $\text{Li}^+$  is no longer in direct hydrogen-bonded contact with a surface, and a DL can form. In this line, we propose that a turnover to a different transport mechanism may occur at separations corresponding to  $> 3$  WL.

## 2.5. NMR Spectroscopy Including Pulsed- and Static-Field Gradient Experiments

The NMR spectroscopic results (Figure 5) for a series of  $[\text{Li}_{0.5}^{\text{inter}}[\text{Mg}_{2.5}\text{Li}_{0.5}]^{\text{oct}}[\text{Si}_4]^{\text{tet}}\text{O}_{10}\text{F}_2]$  powders, swollen with aliquots of water to achieve slit heights between 2.4 Å and 250 Å (Figure S19, Supporting Information), are in excellent agreement with findings of the MD and PB simulations, and the conductivity measurements.

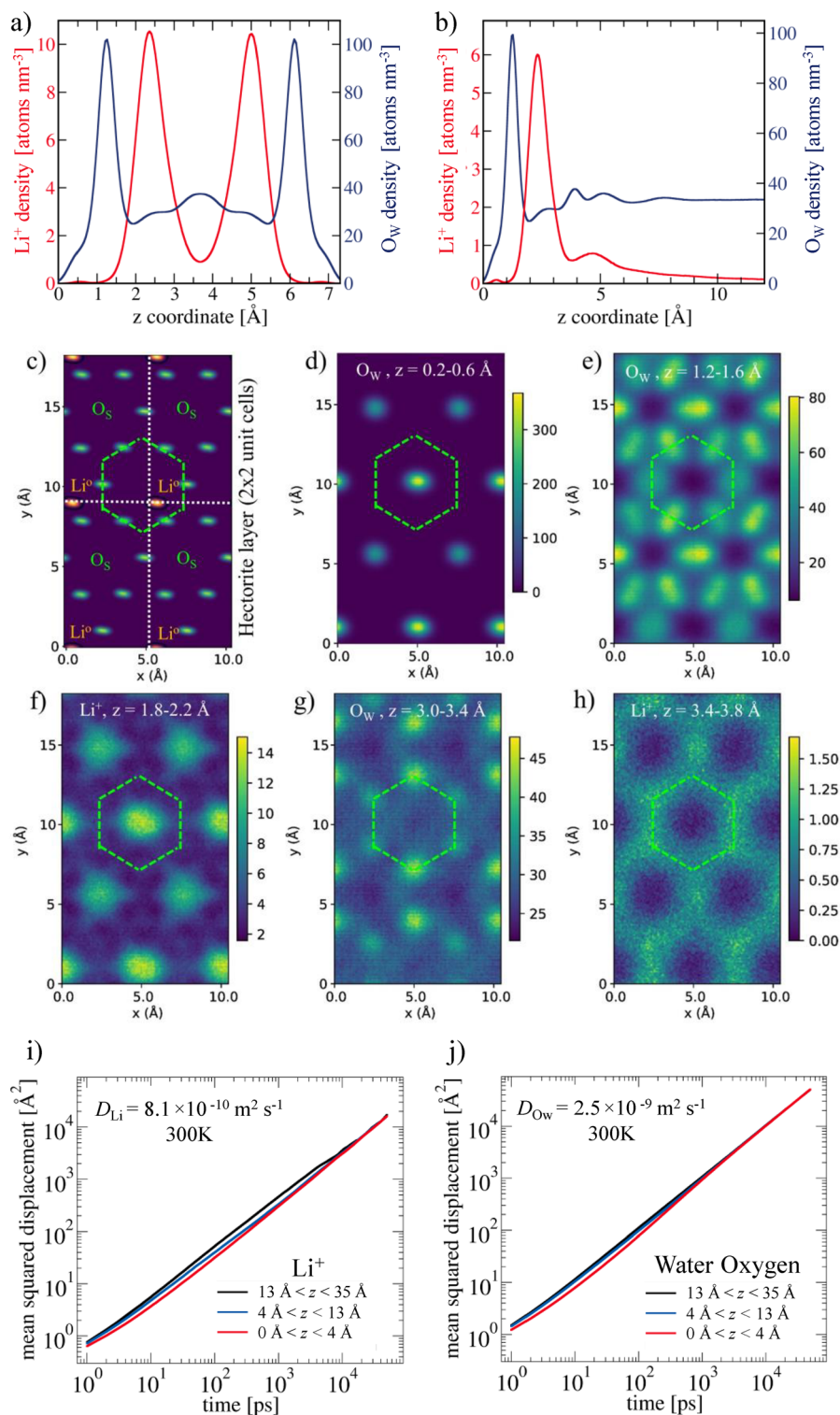


**Figure 4.** Number density profiles  $n_{\text{perp}}(z)$  of  $\text{Li}^+$  (red) and  $\text{O}_W$  (blue) for slit heights of a) 7.2 Å and b) 69 Å. Adding the van der Waals radius to the  $z$ -position defines  $z = 0$ . Number density profiles  $n_{\text{para}}(x, y)$  (in atoms  $\text{nm}^{-3}$ ) for the slit height of 69 Å and the indicated  $z$  regions mapped on a  $2 \times 2$  unit cell of one of the hectorite surfaces: c) surface (basal) oxygens ( $\text{O}_S$ ) and octahedral Li ( $\text{Li}^0$ ) of the 2:1 layered silicate, white dotted lines mark the unit cells, d)  $\text{O}_W$  residing in the hexagonal cavities on the hectorite surface ( $0.2 \text{ \AA} \leq z \leq 0.6 \text{ \AA}$ ), e)  $\text{O}_W$  of 1 WL ( $1.2 \text{ \AA} \leq z \leq 1.6 \text{ \AA}$ ), f)  $\text{Li}^+$  in OHP residing above the hexagonal cavities on the hectorite surface ( $1.8 \text{ \AA} \leq z \leq 2.2 \text{ \AA}$ ), g)  $\text{O}_W$  in 2 WL ( $3.0 \text{ \AA} \leq z \leq 3.4 \text{ \AA}$ ), and h)  $\text{Li}^+$  in DL ( $3.4 \text{ \AA} \leq z \leq 3.8 \text{ \AA}$ ). In c–g) The green dashed lines illustrate the position of one of the hexagonal cavities on the hectorite surface. 2D mean squared displacement  $\langle r_{2D}^2(t) \rangle$  of i)  $\text{Li}^+$  and j)  $\text{O}_W$  residing in the indicated  $z$ -regions at the time of origin. The self-diffusion coefficients  $D$  obtained from the common long-time behavior are shown.

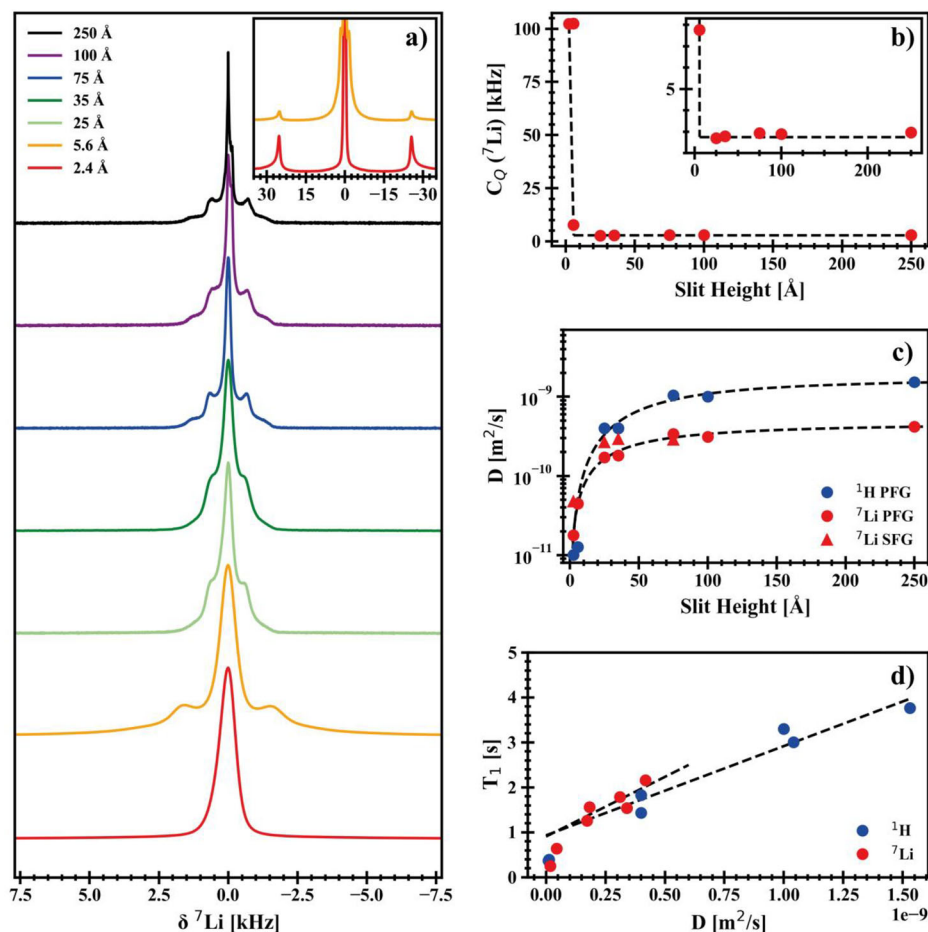


**Figure 5.** a)  $^7\text{Li}$  lineshapes for various slit heights. The inset shows a broader frequency range for slit heights of 2.4 and 5.6 Å to highlight the additional satellites. b) Trend of the  $^7\text{Li}$  quadrupole coupling constant  $C_Q$  as a function of slit height. c)  $^1\text{H}$  and  $^7\text{Li}$  self-diffusion coefficients  $D$  determined with PFG- and SFG-NMR spectroscopy for various slit heights. The dashed lines in b) and c) are guides to the eye. d) Trend for  $T_1$  as a function of  $D$ . The dashed lines in d) are linear fits of the regime where  $T_1$  and  $D$  are proportional.

From the  $^7\text{Li}$  and  $^1\text{H}$  lineshape analysis, two regimes can be differentiated, with a turnover at slit heights between 5.6 Å (2 WL) and 8.5 Å (3 WL) (Figure 5a; Figures S20–S22, Supporting Information). Although satellite transitions are observed for the  $^7\text{Li}$  NMR spectra at all slit heights, the quadrupolar coupling constant ( $C_Q$ , Figure S23, Supporting Information) decreases substantially from 102 kHz at 2.4 Å to 7.8 kHz at 5.6 Å and finally to  $\approx 2.8$  kHz for slit heights  $\geq 25$  Å, where  $C_Q$  becomes slit-height-independent (Figure 5b). A similar trend was observed for the  $^1\text{H}$  lineshapes (Figure S22, Supporting Information). Here, at small slit heights of 2.4 and 5.6 Å, the lineshapes are also broadened anisotropically, giving rise to Pake-type patterns. For larger slit heights, only one narrow Lorentzian peak occurs, which reflects the rising number of water molecules in the slit that are not strongly affected by the hectorite surface. As their number surpasses the number of water molecules near the hectorite surfaces, the average lineshapes are dominated by isotropic contributions.

Due to the fast exchange of  $\text{Li}^+$  and water molecules between HP and DL, the observed spectra reflect the motional average

over these spatial environments. The presence of  $^7\text{Li}$  satellites and anisotropic  $^1\text{H}$  lineshapes is thus primarily governed by the  $\text{Li}^+$  and water molecules residing close to the hectorite surface, where the local asymmetry of the electric field gradient (EFG) is largest, and the local mobility is partially restricted.<sup>[56]</sup> The latter gives rise to  $^1\text{H}$  NMR spectra influenced by residual homonuclear dipolar couplings. For the regime where the conductivity is slit-height-independent, the MD simulation shows that a water layer covers the hectorite surface. As such, all  $\text{Li}^+$ , including the ones in the HP, are fully solvated, explaining the small average  $C_Q$  of  $\approx 2.8$  kHz. The independence of  $C_Q$  from the slit height in this regime further indicates that the  $\text{Li}^+$  distribution over HP and DL does not change significantly, which is in line with the PB simulation.

The substantially increased  $C_Q$  at slit heights smaller than the one applied in the MD simulations (2.4 and 5.6 Å, corresponding to 1 WL and 2 WL, respectively) indicates a different environment for  $\text{Li}^+$ , which is attributed to the occupation of a  $\text{Li}^+$  site in the IHP. As observed in the crystal structure refinement of the 1 WL structure (Figure S5, Supporting Information), the

$\text{Li}^+$  of this site is in direct contact with the hectorite surface by coordinating to six basal oxygens and is only partially solvated by three water molecules. This 6 + 3 coordination environment explains the markedly larger EFGs and the presence of only one pair of satellites for a slit height of 2.4 Å. For a slit height of 5.6 Å, two pairs of satellites are observed. One pair matches the large  $C_Q$  of the 1 WL configuration ( $\approx 102$  kHz) with  $\text{Li}^+$  in a similar coordination. The second pair of satellites is markedly reduced ( $C_Q \approx 7.8$  kHz) but still significantly larger compared to the average ( $C_Q \approx 2.8$  kHz) for larger slit heights. These  $\text{Li}^+$  most likely occupy the octahedral vacancies between two water layers. While the structure of the OHP remains unchanged with increasing slit height, a dynamic exchange occurs at higher slit heights between  $\text{Li}^+$  in the OHP and DL. This exchange is consistent with the MD simulation results (Figure 4i) and explains the observed decrease in  $C_Q$  values, as the exchange between these sub-ensembles is fast compared to the NMR time scale (Figure 5b).

The diffusion coefficients of the water molecules ( $D_{\text{Hw}}$ ) and  $\text{Li}^+$  ( $D_{\text{Li}}$ ) were obtained using  $^1\text{H}$  and  $^7\text{Li}$  PFG- and SFG-NMR experiments. All experimental results confirm the expected 2D geometry of the observed diffusion process (Figure S24, Supporting Information). The  $D_{\text{Hw}}$  values are taken as a measure of water diffusion. A direct comparison of the results from PFG- and SFG-NMR spectroscopy (Figure 5c) reveals that both techniques yield similar  $D$  despite probing different length scales (PFG-NMR: 0.5–20  $\mu\text{m}$ ; SFG-NMR: 0.25–1.3  $\mu\text{m}$ ). This similarity indicates that bottleneck effects, such as transitions between differently oriented stacks or surface inhomogeneities, are negligible, which can be attributed to the nanosheets' large aspect ratio, homogeneous surface charge distribution, and uniform slit heights across the sample. This conclusion is further supported by the observation that the same diffusion coefficient  $D$  is obtained when varying the length scale of SFG diffusion measurements in the range of 100–500  $\mu\text{m}$  (Figure S25, Supporting Information). Moreover,  $D_{\text{Hw}}$  and  $D_{\text{Li}}$  increase with increasing slit heights (Figure 5c) by roughly two orders of magnitude from  $1.0 \times 10^{11}$  to  $1.5 \times 10^9 \text{ m}^2 \text{ s}^{-1}$  and  $1.8 \times 10^{11}$  to  $4.2 \times 10^{-10} \text{ m}^2 \text{ s}^{-1}$  respectively. At a slit height of 250 Å,  $D_{\text{Hw}}$  ( $1.5 \times 10^9 \text{ m}^2 \text{ s}^{-1}$ ) approaches water diffusion coefficients of bulk water ( $D_{\text{HBulk}} = 2.3 \times 10^{-9} \text{ m}^2 \text{ s}^{-1}$ ).<sup>[57]</sup> This trend indicates that the retarded dynamics of the first water layer, which is hydrogen bonded to the basal oxygens of hectorite, rapidly vanish with increasing distance from the hectorite surface, and quasi-bulk-like water dynamics occur within the slit. In contrast, at a slit height of 250 Å,  $D_{\text{Li}}$  ( $4.2 \times 10^{10} \text{ m}^2 \text{ s}^{-1}$ ) is about half of that of  $\text{Li}^+$  in bulk LiCl electrolytes with a concentration equivalent to the  $\text{Li}^+$  concentration within the slit confinement ( $D_{\text{LiBulk}} \approx 1.0 \times 10^{-9} \text{ m}^2 \text{ s}^{-1}$  at RT).<sup>[58]</sup> Clearly, the confinement reduces the conductivity rather than pushing it to superior conductivity. The persistent retardation of  $\text{Li}^+$  dynamics, despite an increasing slit height, also supports our conclusion that the majority of  $\text{Li}^+$  remains close to the charged hectorite surfaces and is thus slowed down by electrostatic interactions and hydrogen bonding to surface oxygen atoms.

For small slit heights ( $\leq 5.6$  Å),  $\text{Li}^+$  diffuses faster than water ( $D_{\text{Li}} > D_{\text{Hw}}$ ), which can be explained by the high degree of order of the water molecules and their hydrogen bonds to the hectorite basal oxygens (Figure S5, Supporting Information). In these highly confined slits,  $\text{Li}^+$  migrates by hopping along octahe-

dral voids of highly ordered water layers. Since water diffusion is slower than that of  $\text{Li}^+$  ions, water molecules form a quasi-solid substructure that facilitates  $\text{Li}^+$  ion transport. Therefore, water molecule and  $\text{Li}^+$  migration occur independently in this regime. The rotational movement of water molecules likely assists the  $\text{Li}^+$  transport. However, because water's rotational dynamics are fast on the NMR time scale, we could not obtain experimental evidence to support this hypothesis. The  $\text{Li}^+$  ion transport mechanism proposed in this regime is more typical of a solid electrolyte than a liquid one.<sup>[54]</sup>

This trend is reversed for larger slit heights, where water diffuses faster than  $\text{Li}^+$  ( $D_{\text{Li}} < D_{\text{Hw}}$ ). We expect the turnover point to be at a slit height of 8 Å with the 3 WL configuration, as the MD model already predicts  $D_{\text{Ow}}$  to be greater than  $D_{\text{Li}}$ . For larger slit heights, all  $\text{Li}^+$  are fully solvated and participate in the diffusion. They will move together with at least the first hydration shell. A portion of the water molecules is therefore coupled to the  $\text{Li}^+$  ions, slowing down the transport of  $\text{Li}^+$  ions and resulting in  $D_{\text{Li}} < D_{\text{Hw}}$  in this regime. This is typical for liquid electrolytes.<sup>[58]</sup>

This mechanistic transition is also reflected in the relationship between spin-lattice relaxation time ( $T_1$ ) and the diffusion coefficients ( $D_{\text{Li}}$  and  $D_{\text{Hw}}$ ), as illustrated in Figure 5d. Assuming that the shape of the spectral density  $J(\omega)$  is independent of slit height,  $D$  and  $T_1$  become proportional for fast, liquid-like motion on the NMR timescale.<sup>[59–61]</sup> While this proportionality is observed at slit heights  $\geq 25$  Å, deviations occur at slit heights  $\leq 5.6$  Å, which is consistent with the confinement-induced changes in the diffusion mechanism, as the transport cannot be described with a liquid-like transport, and the shape of the spectral density may change.

For studying the degree of displacements of different  $\text{Li}^+$  sites in the slit and how they are correlated during transport processes, we compare self-diffusion coefficients obtained from PFG-NMR ( $D_{\text{PFG}}$ ) with those calculated from ionic conductivity using the Nernst-Einstein relation ( $D_{\text{EIS}}$ ) (Figure 6a). While the slit-height-dependence of the diffusion coefficient is consistent across methods,  $D_{\text{PFG}}$  is significantly larger than  $D_{\text{EIS}}$ . The discrepancy likely reflects fundamental differences in what each technique probes. PFG-NMR accesses the self-diffusion of individual ionic species, whereas EIS captures the net charge transport, which is susceptible to interionic correlations, collective effects, and internal polarization.<sup>[62,63]</sup> The relationship between these two types of diffusion coefficients is commonly quantified by the Haven ratio  $H$  ( $H = D_{\text{PFG}}/D_{\text{EIS}}$ ), which is shown as a function of slit height in Figure 6b.

For a Haven ratio of  $H \approx 1$ , ion motion would be uncorrelated and purely stochastic, and the Nernst-Einstein relation would quantify this motion. A Haven ratio of  $H > 1$  indicates destructive cross-correlations among moving ions, where ion pairs or collective motion in opposite directions reduces the net charge transport (EIS) relative to the individual diffusivities (NMR). In strongly confined regimes of the 2 WL with slit heights of  $\leq 5.6$  Å, extraordinarily high Haven ratios of  $H \approx 16$  are observed. This could reflect mobile (as shown by PFG-NMR), but HP localized  $\text{Li}^+$  undergoing frequent local hops and reorientation that are largely ineffective for long-range conductivity.<sup>[64]</sup> At larger slit heights of  $\geq 25$  Å, corresponding to the less confined regime, the Haven ratio levels off to  $H \approx 3$ –4. It indicates that, while still present and relevant, ion-ion correlations are less dominant. The

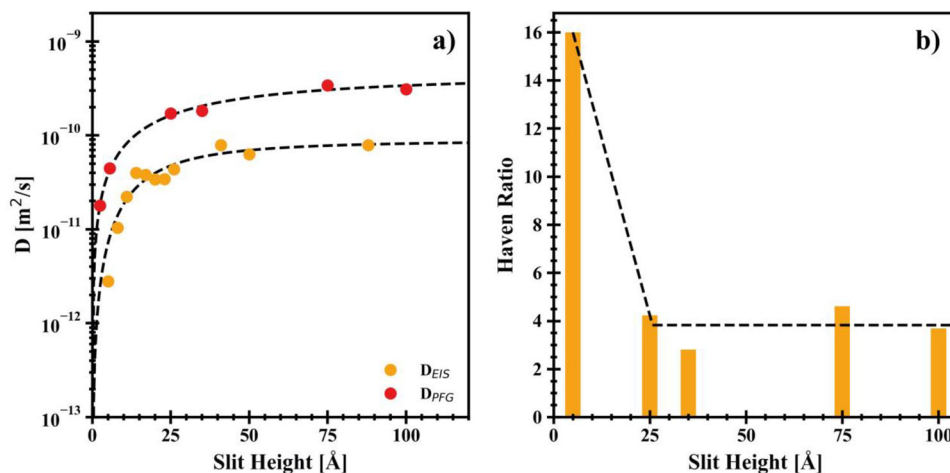


**Figure 6.** a) Comparison of  $\text{Li}^+$  diffusion coefficients obtained using PFG-NMR spectroscopy ( $D_{\text{PFG}}$ ) and EIS ( $D_{\text{EIS}}$ ).  $D_{\text{EIS}}$  was derived from the conductivity using the Nernst-Einstein relation. b) Haven ratios for various slit heights. For slit heights  $> 100 \text{ Å}$ , where  $D_{\text{PFG}}$  is not matched with a data point from impedance spectroscopy, the  $D_{\text{EIS}}$  were interpolated linearly.

change further suggests that  $\text{Li}^+$  becomes decoupled from the surface, transitioning toward more bulk-like (though still confined) transport. In this regime, the ionic distribution is less sensitive to slit height, as the relative populations in the HP and DL change only insignificantly.

## 2.6. Intrinsic versus Extrinsic $\text{Li}^+$ Concentrations and Debye Length

So-called “surface charge dominated conductivity”, as implied by the slit confinement of negatively charged hectorite nanosheets, allows only counter-cations to the surface charge to enter the slit at low to moderate heights. The number of intrinsic counterions is bound by the charge neutrality requirement. Thus, when swelling with bidest. water, the cation number within the slit must be constant for a given degree of isomorphous substitution (e.g., for  $\text{Li}_{0.5}\text{Hec}$ ,  $2.15 \text{ Li}^+ \text{ nm}^{-2}$ ), regardless of the slit height. Additionally, when considering electrolytes containing both anions and cations, the incorporation of anions between negatively charged nanosheets is restricted due to charge exclusion<sup>[65–67]</sup> and ion rectification.<sup>[68]</sup>

When increasing the slit height with bidest. water, the number of interlayer cations remains constant while consequently decreasing their concentration within the slit. This concentration of intrinsic  $\text{Li}^+$  within the slit can be calculated for any given slit height of  $\text{Li}_{0.5}\text{Hec}$  (Figure S6, Supporting Information) as 7.1, 3.6, 2.4, and  $0.4 \text{ mol L}^{-1}$  for slit heights of 5, 10, 15, and 100  $\text{Å}$ , respectively. This concentration is substantially higher than the concentration of the swelling electrolyte solution (0.1–100 mM) (Figure 2b), suggesting that the conductivity in the confinement is primarily dominated by the larger number of intrinsic interlayer cations, even at slit heights surpassing twice the Debye length. This is interesting, as the Debye length, which is dependent on ionic strength, was often named a governing or limiting length scale for surface-charged or confined ionic transport.<sup>[24,69]</sup> Hence, the surface conductivity originates primarily from the stagnant layer of closely bound ions at the surfaces rather than

from the overlapping diffuse layers. The different contributions to surface conductivity are an effect that has been studied previously for other systems.<sup>[70,71]</sup> Even at an electrolyte concentration of 100 mM, where the Debye length is 10  $\text{Å}$ , the conductivity remained dominated by surface charges rather than electrolyte concentration. This effect was true even when the slit height was sufficiently large (e.g., 80  $\text{Å}$ ), where the HPs and the Debye lengths of both surfaces no longer overlapped. For this reason, the effect of salt concentration on the conductivity is further examined in the next section.

## 2.7. Separations Far Beyond the Debye Length

The Wigner crystal starts ‘melting’ when the interlayer separation reaches the Debye length, where electrostatic interactions between adjacent layers are screened by a large. The layers become weakly charge-correlated, which is indicated by fulfilling the classical Hansen-Verlet and Lindeman criteria for melting.<sup>[45]</sup> Nevertheless, due to the 20  $\mu\text{m}$  diameter of the hectorite nanosheets, they are still forced into a coplanar arrangement within the nematic liquid crystalline domains, even when separated to  $> 200 \text{ nm}$ , leading to structural colors.<sup>[72]</sup> While preparation of monodomain membranes is no longer possible at this stage, confinement can be extended to significantly larger slit heights of  $> 100 \text{ nm}$  by swelling with appropriate aliquots of water.<sup>[73]</sup> A compromise to be accepted is that only randomly oriented domains, instead of textured membranes, are accessible. Measurable, averaged slit heights of 180 nm (SAXS) and 600 nm (Spectral Data) were previously achieved by dilution.<sup>[72]</sup> Diluting beyond 600 nm should result in a further increase in slit height, following the previously observed relationship of the suspension volume fraction ( $\phi$ ) and the slit height, of  $\phi^{-0.66}$ .<sup>[45]</sup> As slit heights  $> 600 \text{ nm}$  cannot be confirmed experimentally, they were calculated from their respective dilution. The ionic conductivity of such diluted nematic suspensions was determined via EIS. The preparation of these suspensions followed the previously described protocols.<sup>[72]</sup>

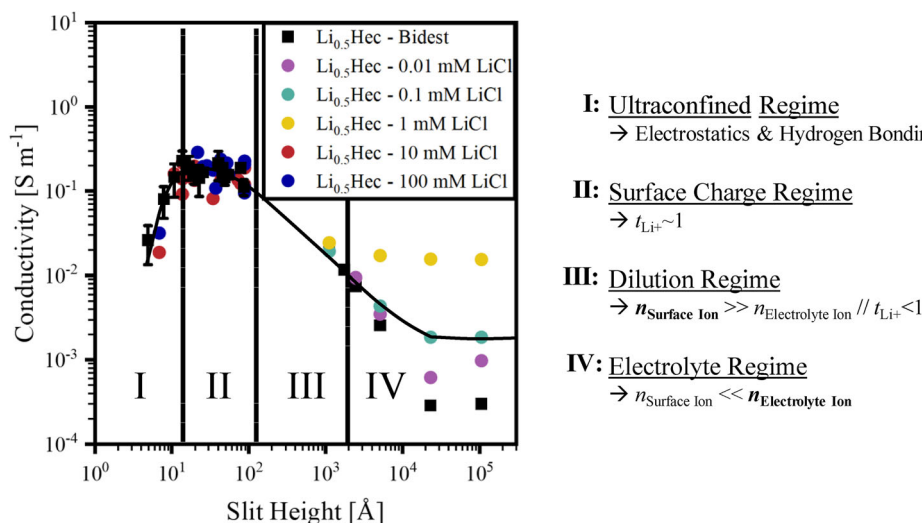


**Figure 7.** Four distinct regimes of ionic conductivity as a function of slit height may be identified. Regimes I and II correspond to in situ measurements on monodomain textured membranes. Regimes III and IV were measured with aqueous nematic suspensions. I) Ultraconfined regime:  $\text{Li}^+$  is immobilized by electrostatics and hydrogen bonding of the first coordination shell to the hectorite surface. II) Confined regime: Ionic conductivity is dominated by  $\text{Li}^+$  concentration balancing the negative surface charge of the hectorite. A plateau arises as the number of  $\text{Li}^+$  in the DL increases while their concentration decreases with further dilution. III) Dilution regime: The population of the DL with  $\text{Li}^+$  has reached its maximum and is subsequently only diluted with increasing slit height. Surface charge carriers remain the dominant contributors to conductivity, exceeding the contribution from bulk electrolyte ions. IV) Electrolyte regime: Conductivity is dominated by bulk electrolyte ions when  $n_{\text{Surface}} < n_{\text{Electrolyte}}$ .

With respect to ionic conductivity, four distinct regimes of slit heights can be identified that differ in their effect on surface-charge-governed nanochannel conductivity (Figure 7). For these regimes, only the surface charges and the volume of electrolyte within the slit are considered. In the ultraconfined regime (I),  $\text{Li}^+$  is immobilized by electrostatics and hydrogen bonding of the first coordination shell. Next, the surface charge-governed regime (II) follows, where conductivity reaches its maximum before entering a plateau. Here, the conductivity is dictated by the surface charge density, and  $\text{Li}^+$  is distributed over the HP and DL. In this regime, as the slit height increases, the number of  $\text{Li}^+$  in the DL, remote from the surface, also increases. Thus, as the slit height (and slit volume) increases, the conductivity is governed by a balance of an increasing absolute number of  $\text{Li}^+$  in the DL and a decreasing concentration of  $\text{Li}^+$  within the slit. In the surface charge dilution regime (III), the number of  $\text{Li}^+$  in the DL no longer increases. Consequently, as the slit height increases further, the conductivity decreases because the  $\text{Li}^+$  concentration within the slit decreases. At this stage, the  $\text{Li}^+$  concentration required for charge neutrality still outnumbers the charge carriers contributed by the electrolyte. Finally, bulk electrolyte charge carriers outnumber surface charges in the electrolyte-governed conductivity regime (IV). The conductivity is constant, becomes independent of slit height, and depends solely on the electrolyte concentration. Higher electrolyte concentrations reach this regime at smaller slit heights. These four regimes define the relationship between slit height, surface charge, and nanochannel conductivity.

### 3. Conclusion

Reports of superior conductivity in 2D slit confinement of clays revealed a complex interplay of confinement geometry, ion-ion

correlations, and material properties like charge density of confining walls. Strong electrostatic correlations and dehydration effects dominate, leading to suppressed or highly nonlinear transport. Rather than being a simple function of dimensionality, superionic conductivity in 2D slit confinement is a material- and structure-dependent phenomenon.

This study of  $\text{Li}^+$  and water dynamics in fluorohectorite Bragg stack membranes establishes a new benchmark for the systematic study of ion transport in 2D nanofluidic channels, leveraging Å-precision control, multimodal characterization, and advanced modeling. By mapping out the full range of confinement regimes and elucidating the corresponding changes in transport mechanism, from suppressed hopping in ultraconfinement, through a transition to liquid-like diffusion, to dilution-limited conductivity at large slit heights this study provides a unified framework connecting microscopic structure, ion distribution, and macroscopic transport.

Key advances over the literature include: 1) Direct experimental confirmation and mechanistic understanding that the 2D conductivity as a function of the slit height is governed by two regimes, with a crossover occurring when the slit height exceeds three water layers. Below this slit height,  $\text{Li}^+$  diffusion is driven by hopping between voids formed by quasi-static water molecules ( $D_{\text{Li}} > D_{\text{Hw}}$ ), which is typical for solid electrolytes. In this case, the migration of  $\text{Li}^+$  and water molecules occurs independently. Above the critical slit height,  $\text{Li}^+$  moves together with a hydration sphere of water molecules, similar to what happens in a liquid electrolyte. In this regime, some water molecules are coupled to  $\text{Li}^+$  transport, resulting in  $D_{\text{Li}} < D_{\text{Hw}}$ . 2) Demonstration that surface charge effects dominate ion transport well beyond the Debye length, challenging conventional screening-based models and highlighting the importance of intrinsic counterions in nanoconfined systems. 3) Quantitative analysis of ion-ion

correlations via Haven ratios, revealing the profound impact of correlated motion and local structure on macroscopic conductivity. 4) Validation of theoretical and simulation predictions regarding water and ion layering and their control over transport properties.

This work not only deepens the fundamental understanding of ion transport under extreme confinement but also provides a robust experimental and theoretical platform for validating and refining nanofluidic transport theories. The insights gained will inform the rational design of next-generation ion-conductive materials for energy storage, separation, and sensing applications, where precise control of channel architecture and surface chemistry can be harnessed to optimize performance across diverse operational regimes. The ability to exploit or mitigate strong ion-ion correlations, control dehydration barriers, and engineer nanochannel architectures opens new avenues for advanced materials design in energy storage, filtration, and nanofluidic devices. Future work should focus on elucidating the microscopic mechanisms governing these effects and leveraging them for practical applications in solid-state batteries, fuel cells, and next-generation iontronic devices. Key to improved performance of clay confinement will be increasing the  $\text{Li}^+$  in the diffuse layer over the one in the Helmholtz planes. Work in this direction is in progress.

#### 4. Experimental Section

Details of the experimental and methodological part can be found in the Supporting Information.

#### Supporting Information

Supporting Information is available from the Wiley Online Library or from the author.

#### Acknowledgements

The authors thank Markus Retsch for making the software COMSOL Multiphysics and CLSM equipment available. The authors acknowledge Marco Schwarzmann, Daniel Hohenberger, Michael Thelen, Florian Puchtler, Beate Bojer, and René Siegel for technical support and synthesizing the materials. The authors gratefully acknowledge the support and funding by the German Research Foundation (DFG) within CRC 1585 (project number 492723217) for subprojects A04 and A05. Support by the BayBatt Cell Technology Center is gratefully acknowledged, which was funded by the Deutsche Forschungsgemeinschaft (DFG, German Research Foundation)—INST 91/452-1 LAGG.

#### Conflict of Interest

The authors declare no conflict of interest.

#### Author Contributions

M.S., S.P., L.K., A.N., and J.K.P. contributed equally to this work. J.B., G.P., M.V., and J.S. conceived the idea, designed the experiments, and supervised the project. M.S. conducted and designed the experiments applying nematic fluorohectorite phases and measured EIS. L.K. conducted the

CP-AFM characterization of nanosheets. S.P. and J.K.P. collected and interpreted NMR data. A.N. designed and interpreted the MD simulations. M.R. assisted with the MD simulations and SFG-NMR experiments. F.L. contributed to the COMSOL Multiphysics simulations. S.W. helped with the initial design of the cell. M.S., S.P., L.K., M.V., A.N., and J.K.P. prepared the figures. M.S., S.P., L.K., A.N., and J.K.P. wrote the manuscript with input from others, and J.B., G.P., M.V., and J.S. polished the final version.

#### Data Availability Statement

The data that support the findings of this study are available in the supplementary material of this article.

#### Keywords

2D materials, lithium-ion conductivity, mobility in confinement, nanochannels, slit confinement

Received: June 19, 2025

Revised: August 6, 2025

Published online:

- [1] H. Zhang, Y. Tian, L. Jiang, *Nano Today* **2016**, *1*, 61.
- [2] P. Sharma, T. Sana, S. Khatoun, U. M. Naikoo, Mosina, N. Malhotra, M. d. S. Hasnain, A. K. Nayak, J. Narang, *Anal. Biochem.* **2025**, *61*, 115791.
- [3] Y. Wang, Y. Zhao, A. Bollas, Y. Wang, K. F. Au, *Nat. Biotechnol.* **2021**, *11*, 1348
- [4] Z. Liu, Z. Ma, X. Wang, D. Ye, H. Yu, J. H. Xin, *Desalination* **2022**, *537*, 115876.
- [5] Z. Liu, Z. Ma, B. Qian, A. Y. H. Chan, X. Wang, Y. Liu, J. H. Xin, *ACS Nano* **2021**, *9*, 15294
- [6] T. Foller, X. Wen, Y. Y. Khine, D. Ji, T. Gupta, M. Muller, C. Scret, R. Joshi, *J. Membr. Sci.* **2023**, *686*, 122022.
- [7] X. Ren, D. Ji, X. Wen, H. Bustamante, R. Daiyan, T. Foller, Y. Y. Khine, R. Joshi, *J. Mater. Res.* **2022**, *20*, 3362
- [8] X. Jiang, L. Wang, S. Liu, F. Li, J. Liu, *Mater. Chem. Front.* **2021**, *4*, 1610
- [9] S. Lin, Y. Liu, J. Hu, F. Xia, X. Lou, *Chem. Commun.* **2025**, *10*, 1978
- [10] R. C. Massé, C. Liu, Y. Li, L. Mai, G. Cao, *Natl. Sci. Rev.* **2017**, *1*, 26.
- [11] J. K. Lee, F. Babbe, G. Wang, A. W. Tricker, R. Mukundan, A. Z. Weber, X. Peng, *Joule* **2024**, *8*, 2357.
- [12] Y. Jiao, C. Yang, W. Zhang, Q. Wang, C. Zhao, *Renew. Sustain. Energy Rev.* **2024**, *191*, 114078.
- [13] A. Fanget, F. Traversi, S. Khybov, P. Granjon, A. Magrez, L. Forró, A. Radenovic, *Nano Lett.* **2014**, *1*, 244
- [14] C. Li, X. Guan, Y. Sun, J. Li, *Anal. Sens.* **2022**, *6*, 202200031.
- [15] C. J. Porter, J. R. Werber, M. Zhong, C. J. Wilson, M. Elimelech, *ACS Nano* **2020**, *14*, 10894.
- [16] S. Wang, L. Yang, G. He, B. Shi, Y. Li, H. Wu, R. Zhang, S. Nunes, Z. Jiang, *Chem. Soc. Rev.* **2020**, *4*, 1071
- [17] X. Yu, W. Ren, *Nat. Commun.* **2023**, *1*, 3998
- [18] J. Liang, Y. Wu, Z. Sun, C. Zeng, Y. Liu, Y. Zhao, T. Zhai, H. Li, *Energy Environ. Sci.* **2024**, *9*, 3210.
- [19] M. Zeng, Y. Xiao, J. Liu, K. Yang, L. Fu, *Chem. Rev.* **2018**, *118*, 6236.
- [20] J. Wang, H. Zhou, S. Li, L. Wang, *Angew. Chem., Int. Ed.* **2023**, *19*, 202218321.
- [21] X. Yu, W. Ren, *Adv. Funct. Mater.* **2024**, *30*, 2313968.
- [22] S. Kim, H. Choi, B. Kim, G. Lim, T. Kim, M. Lee, H. Ra, J. Yeom, M. Kim, E. Kim, J. Hwang, J. S. Lee, W. Shim, *Adv. Mater.* **2023**, *43*, 2206354.
- [23] H. Zhan, Z. Xiong, C. Cheng, Q. Liang, J. Z. Liu, D. Li, *Adv. Mater.* **2020**, *18*, 1904562.

- [24] N. Kavokine, R. R. Netz, L. Bocquet, *Annu. Rev. Fluid Mech.* **2021**, *53*, 377.
- [25] H.-C. Chang, L. Y. Yeo, in *Electrokinetically-Driven Microfluidics and Nanofluidics*, Cambridge University Press & Assessment, Cambridge, UK **2010**.
- [26] D. Stein, M. Kruithof, C. Dekker, *Phys. Rev. Lett.* **2004**, *3*, 035901.
- [27] B. Radha, A. Esfandiari, F. C. Wang, A. P. Rooney, K. Gopinadhan, A. Keerthi, A. Mishchenko, A. Janardanan, P. Blake, L. Fumagalli, M. Lozada-Hidalgo, S. Garaj, S. J. Haigh, I. V. Grigorieva, H. A. Wu, A. K. Geim, *Nature* **2016**, *7624*, 222.
- [28] H. Zhang, Y. Zheng, S. Yu, W. Chen, J. Yang, *Nanomaterials* **2022**, *12*, 2103.
- [29] J.-J. Shao, K. Raidongia, A. R. Koltonow, J. Huang, *Nat. Commun.* **2015**, *1*, 7602
- [30] T. J. Konch, R. K. Gogoi, A. Gogoi, K. Saha, J. Deka, K. A. Reddy, K. Raidongia, *Mater. Chem. Front.* **2018**, *9*, 1647
- [31] Z. Huang, Y. Zhang, T. Hayashida, Z. Ji, Y. He, M. Tsutsui, X. S. Miao, M. Taniguchi, *Appl. Phys. Lett.* **2017**, *111*, 263104.
- [32] L. i. Ding, D. Xiao, Z. Lu, J. Deng, Y. Wei, J. Caro, H. Wang, *Angew. Chem.* **2020**, *22*, 8798.
- [33] F. Xian, L. Jia, Y. Sugahara, H. Xue, Y. Yamauchi, T. Sasaki, R. Ma, *ACS Appl. Mater. Interfaces* **2022**, *45*, 51212.
- [34] Z. Zhang, L. Wen, L. Jiang, *Nat. Rev. Mater.* **2021**, *7*, 622.
- [35] N. Li, Y. Xie, S. Peng, X. Xiong, K. Han, *J. Energy Chem.* **2020**, *42*, 116.
- [36] W. Kong, L. Yan, Y. Luo, D. Wang, K. Jiang, Q. Li, S. Fan, J. Wang, *Adv. Funct. Mater.* **2017**, *18*, 1606663.
- [37] A.-K. Hatz, I. Moudrakovski, S. Bette, M. W. Terban, M. Etter, M. Joos, N. M. Vargas-Barbosa, R. E. Dinnebier, B. V. Lotsch, *Chem. Mater.* **2021**, *18*, 7337.
- [38] P. D. Kaviratna, T. J. Pinnavaia, P. A. Schroeder, *J. Phys. Chem. Solids* **1996**, *12*, 1897.
- [39] V. Dudko, O. Khoruzhenko, S. Weiß, M. Daab, P. Loch, W. Schwieger, J. Breu, *Adv. Mater. Technol.* **2023**, *3*, 2200553.
- [40] J. Breu, W. Seidl, A. J. Stoll, K. G. Lange, T. U. Probst, *Chem. Mater.* **2001**, *11*, 4213.
- [41] H. Kalo, M. W. Möller, M. Ziadeh, D. Dolejš, J. Breu, *Appl. Clay Sci.* **2010**, *1*, 39.
- [42] J. N. Israelachvili, R. M. Pashley, *Nature* **1983**, *5940*, 249.
- [43] R. M. Pashley, J. N. Israelachvili, *J. Colloid Interface Sci.* **1984**, *2*, 511.
- [44] A. Esfandiari, B. Radha, F. C. Wang, Q. Yang, S. Hu, S. Garaj, R. R. Nair, A. K. Geim, K. Gopinadhan, *Science* **2017**, *6362*, 511.
- [45] S. Rosenfeldt, M. Stöter, M. Schlenk, T. Martin, R. Q. Albuquerque, S. Förster, J. Breu, *Langmuir* **2016**, *41*, 10582.
- [46] P. D. Kaviratna, T. J. Pinnavaia, P. A. Schroeder, *J. Phys. Chem. Solids* **1996**, *12*, 1897.
- [47] T. J. Senden, *Curr. Opin. Colloid Interface Sci.* **2001**, *2*, 95.
- [48] H.-J. Butt, B. Cappella, M. Kappl, *Surf. Sci. Rep.* **2005**, *1*, 1.
- [49] V. Kuznetsov, K. Ottermann, N. Helfrich, D. Kunz, P. Loch, H. Kalo, J. Breu, G. Papastavrou, *Colloid Polym. Sci.* **2020**, *7*, 907.
- [50] R. Pericet-Camara, G. Papastavrou, S. H. Behrens, M. Borkovec, *J. Phys. Chem. B* **2004**, *50*, 19467.
- [51] R. Pericet-Camara, G. Papastavrou, S. H. Behrens, C. A. Helm, M. Borkovec, *J. Colloid Interface Sci.* **2006**, *2*, 496.
- [52] L. J. Kirwan, P. Maroni, S. H. Behrens, G. Papastavrou, M. Borkovec, *J. Phys. Chem. B* **2008**, *46*, 14609.
- [53] J. N. Israelachvili, in *Intermolecular and Surface Forces*, Academic Press, San Diego, California **2011**.
- [54] B. Rotenberg, V. Marry, J.-F. Dufrêche, N. Malikova, E. Giffaut, P. Turq, *C. R. Chim.* **2007**, *10*, 1108.
- [55] J. A. Greathouse, D. B. Hart, G. M. Bowers, R. J. Kirkpatrick, R. T. Cygan, *J. Phys. Chem. C* **2015**, *30*, 17126.
- [56] G. Trausch, D. Canet, P. Turq, *Chem. Phys. Lett.* **2008**, *4*, 262.
- [57] M. Holz, S. R. Heil, A. Sacco, *Phys. Chem. Chem. Phys.* **2000**, *20*, 4740.
- [58] H. G. Hertz, R. Tutsch, H. Versmold, *Ber. Bunsenges. Phys. Chem.* **1971**, *11*, 1177.
- [59] N. Bloembergen, E. M. Purcell, R. V. Pound, *Phys. Rev.* **1948**, *7*, 679.
- [60] V. Overbeck, A. Appelhagen, R. Rößler, T. Niemann, R. Ludwig, *J. Mol. Liq.* **2021**, *322*, 114983.
- [61] D. Kruk, R. Meier, E. A. Rössler, *J. Phys. Chem. B* **2011**, *5*, 951.
- [62] A. C. Lazanas, M. I. Prodromidis, *ACS Meas. Sci. Au* **2023**, *3*, 162.
- [63] M. E. Orazem, B. Tribollet, *ChemTexts* **2020**, *2*, 12
- [64] K. Hogrefe, N. Minafra, I. Hanghofer, A. Banik, W. G. Zeier, H. M. R. Wilkening, *J. Am. Chem. Soc.* **2022**, *4*, 1795
- [65] S. Wang, Y. i. Huang, Y. u. Qiang, M. Wu, S. Liang, J. Wang, C. Fang, L. Zhu, *Water Res.* **2025**, *270*, 122855.
- [66] A. Plecis, R. B. Schoch, P. Renaud, *Nano Lett.* **2005**, *6*, 1147.
- [67] R. B. Schoch, H. van Lintel, P. Renaud, *Phys. Fluids* **2005**, *10*, 100604.
- [68] J. Rabinowitz, M. A. Edwards, E. Whittier, K. Jayant, K. L. Shepard, *J. Phys. Chem. A* **2019**, *38*, 8285.
- [69] K. Xiao, L. Jiang, M. Antonietti, *Joule* **2019**, *10*, 2364.
- [70] R. Zimmermann, J. F. L. Duval, C. Werner, *Curr. Opin. Colloid Interface Sci.* **2019**, *44*, 177.
- [71] J. Lyklema, *J. Phys.: Condens. Matter* **2001**, *13*, 5027.
- [72] P. H. Michels-Brito, V. Dudko, D. Wagner, P. Markus, G. Papastavrou, L. Michels, J. Breu, J. O. Fossum, *Sci. Adv.* **2022**, *4*, abl8147.
- [73] C. Liang, V. Dudko, O. Khoruzhenko, X. Hong, Z.-P. Lv, I. Tunn, M. Umer, J. V. I. Timonen, M. B. Linder, J. Breu, O. Ikkala, H. Zhang, *Nat. Mater.* **2025**, *4*, 599.